

NASA/CR-2000-209870  
ICASE Report No. 2000-10



## **Nondestructive Evaluation Using a Reduced Order Computational Methodology**

*Michele L. Joyner and H.T. Banks*  
*North Carolina State University, Raleigh, North Carolina*

*Buzz Wincheski and William P. Winfree*  
*NASA Langley Research Center, Hampton, Virginia*

*Institute for Computer Applications in Science and Engineering*  
*NASA Langley Research Center*  
*Hampton, VA*

*Operated by Universities Space Research Association*



National Aeronautics and  
Space Administration

Langley Research Center  
Hampton, Virginia 23681-2199

Prepared for Langley Research Center  
under Contract NAS1-97046

March 2000

# NONDESTRUCTIVE EVALUATION USING A REDUCED ORDER COMPUTATIONAL METHODOLOGY\*

MICHELE L. JOYNER<sup>†</sup>, H. T. BANKS<sup>‡</sup>, BUZZ WINCHESKI<sup>§</sup>, AND WILLIAM P. WINFREE<sup>¶</sup>

**Abstract.** This paper uses eddy current based techniques and reduced order modeling to explore the feasibility of detecting a subsurface damage in structures such as air foils and pipelines. To identify the geometry of a damage, an optimization algorithm is employed which requires solving the forward problem numerous times. To implement these methods in a practical setting, the forward algorithm must be solved with extremely fast and accurate solution methods. Therefore, our computational methods are based on the reduced order Karhunen-Loeve or Proper Orthogonal Decomposition (POD) techniques. For proof-of-concept, we implement the methodology on a 2-D problem and find the methods to be efficient and robust even with data containing 10% relative noise. Furthermore, the methods are fast; our findings suggest we can reduce the computational time on average by a factor of 3000.

**Key words.** reduced order modeling, nondestructive evaluation, eddy current methods

**Subject classification.** Applied & Numerical Mathematics

**1. Introduction and Problem Formulation.** In the field of nondestructive evaluation, new and improved techniques are constantly being sought to facilitate the detection of hidden corrosion and flaws in structures such as air foils and pipelines. Many electromagnetic techniques and instruments already exist to aid in the detection of hidden flaws and corrosion. Some of the devices and techniques in use today involve the magneto-optic/eddy current imager [11, 28] in conjunction with eddy current imaging [12, 13], the self-nulling eddy current probe [31] along with conformal mapping techniques [32], and the SQUID (Superconducting Quantum Interference Device) through the use of either injected current methods or induced eddy current methods [7, 9, 15, 25, 27, 30]. We attempt to contribute to these techniques already in use by decreasing the computational time required to detect and explicitly characterize a damage in a material. In other words, given data obtained from a measuring device, we seek to locate and parameterize the damage while minimizing the amount of time required to complete this task. To this end, we formulate and develop an appropriate inverse problem approach and present computational methods along with numerical results to support the efficacy of our approach.

The proposed computational approach is based on approximation ideas from the Karhunen-Loeve or Proper Orthogonal Decomposition (POD) reduced order methodology. Recently these techniques have been successfully used in reduced order methodologies for feedback control design [1, 2, 8, 17, 20] as well as open

---

\*This research was partially supported by the National Aeronautics and Space Administration under NASA Contract No. NAS1-97046 while the first two authors were in residence at the Institute for Computer Applications in Science and Engineering (ICASE), NASA Langley Research Center, Hampton, VA 23681-2199.

<sup>†</sup>Center for Research in Scientific Computation, North Carolina State University, Box 8205, Raleigh, NC 27695-8205. This research was supported in part by the NASA Langley Graduate Researcher's Program under Grant NGT-1-52196, in part by the Air Force Office of Scientific Research under Grant AFOSR F49620-98-1-0430, and in part under Grant AFOSR F49620-98-1-0180.

<sup>‡</sup>Center for Research in Scientific Computation, North Carolina State University, Box 8205, Raleigh, NC 27695-8205. This research was supported in part under Grant AFOSR F49620-98-1-0180.

<sup>§</sup>Mail Stop 231, 4 Langley Boulevard, NASA Langley Research Center, Hampton, VA 23681-2199.

<sup>¶</sup>Mail Stop 231, 4 Langley Boulevard, NASA Langley Research Center, Hampton, VA 23681-2199.

loop control design [24]. Here we propose for the first time the use of such techniques in electromagnetic based damage detection problems. Initial findings reported below are most encouraging.

The only other reference (to our knowledge) in which POD reduced order model techniques are used in conjunction with inverse problems is [29] in which the authors seek to reconstruct distributed conductivities from surface voltage measurements in the classical electrical impedance tomography problem.

**1.1. Description of Problem.** Depending upon the application, different measuring devices and techniques are used in nondestructive evaluation. An advanced method of damage detection uses a device such as the SQUID or self-nulling probe as the sensor for eddy current methods. One way in which the eddy current method is implemented is by placing a thin conducting sheet carrying a uniform current above or below the sample. The current within the sheet induces a magnetic field perpendicular to it that in turn produces a current within the sample, called an eddy current. When a flaw is present within the sample, the flaw disrupts the eddy current flow near the flaw and this disturbance is manifested in the magnetic flux density detected by the measuring device. Using these measurements of the magnetic flux density, we attempt to reconstruct the geometry and location of the flaw explicitly.

To test the feasibility of reconstructing the geometry of the damage, we consider a two-dimensional problem in which the damage (which we shall refer to as a “crack”) is rectangular in shape. In the two-dimensional problem, we assume we have uniformity in the direction of the current flow in the conducting sheet which we label the  $z$  direction, denoting the width of the sample. The  $x$  direction denotes the length of the sample while the  $y$  direction denotes the thickness of the sample. To further simplify the test problem, we disregard the boundary effects of the materials in the  $x$  direction (sample length) by assuming an infinite sample and conducting sheet in that direction. If the conducting sheet and sample are not of infinite extent, we have to take into account the discontinuities in the current flow at the boundaries. Because we are considering materials of infinite extent, we will construct our forward problem by focusing on a small “window”. We will center this “window” such that the left boundary of the “window”, at location  $x = 0$ , is positioned in the center of the crack in the  $x$  direction, i.e., the crack is symmetric through the  $yz$  plane at  $x = 0$ . Therefore, at both the left and right boundaries of the “window” we assume evenly symmetric boundary conditions to account for the symmetry of the crack as well as the infinite extent of the sample and conducting sheet in the  $x$  direction. A schematic of the resulting two-dimensional problem is depicted in Fig. 1.1 where it is assumed that the sample (which is  $20mm$  thick) is composed of aluminum and the conducting sheet (which is  $0.1mm$  thick) is made up of copper and the crack is centered in the  $y$  direction around the center of the sample (i.e., around  $y = -10mm$ ).

Although certain simplifications are made in the two-dimensional case, the two-dimensional analysis is relevant to special three-dimensional cases. In a “true” three-dimensional case, the sample will be of finite length (finite in the  $x$  direction). However, if the crack is located “far enough” away from the boundaries of the sample in the  $x$  direction, we can assume the boundary effects are not sufficiently significant to effect the measurements taken by a SQUID (or similar device). Therefore, the infinite extent of the sample in the test problem will fairly accurately portray the finite sample in the three dimensional case. Similarly, in the two-dimensional test problem, we assume the sample along with the damage or crack to have an infinite width. However, in the three-dimensional case, the crack will have a finite width. To account for this, we assume that data will be taken by scanning along the length of the sample on a line fixed at a certain height using a SQUID. If the line upon which we are scanning is fixed in the  $z$  direction (along the width of the sample) so that the line is “far enough” away from the edges of the crack in the  $z$  direction (along the width of the crack), we should still be able to use the two-dimensional analysis to determine the feasibility

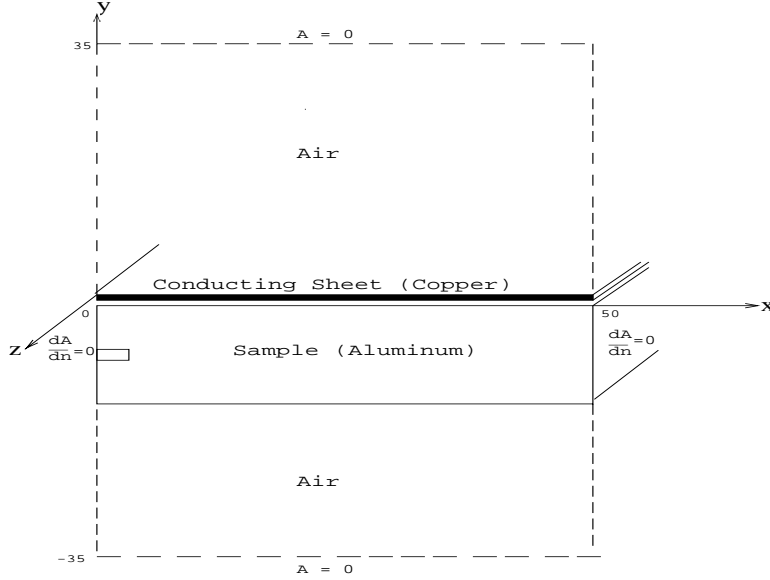


FIG. 1.1. 2-D Schematic of Problem

of identifying length, thickness and depth of the crack in the sample with SQUID data.

**1.2. The Use of Phasors.** As mentioned in the previous section, a conducting sheet (copper in our example) carrying a uniform current is placed above the sample to induce eddy currents within the sample. Without loss of generality, we assume the source current has the form

$$\bar{\mathbf{J}}_s = J_s \cos(\omega t) \hat{\mathbf{k}} = J_s \text{Re}(e^{i\omega t}) \hat{\mathbf{k}}.$$

This current produces a magnetic field  $\bar{\mathbf{H}}(x, y, t)$  described by Maxwell's equations. At the surface of the sample, the magnetic field has the same time dependence as the source current,

$$\bar{\mathbf{H}}(x, y, t) = \tilde{\mathbf{H}}(x, y) \cos(\omega t).$$

However, as the magnetic field penetrates into the sample, a phase lag results due to the finite conductivity of the sample (aluminum in our example). In other words, the magnetic field takes the form

$$\bar{\mathbf{H}}(x, y, t) = \tilde{\mathbf{H}}(x, y) \cos(\omega t + \theta(x, y)),$$

where the term  $\theta(x, y)$  takes into account the depth of penetration. Hence,  $\tilde{\mathbf{H}}(x, y)$  is a vector field quantity which keeps track of the magnitude and direction of  $\bar{\mathbf{H}}$  at each point in space while  $\theta(x, y)$  denotes the phase shift from the original cosine wave at the same point in space. Consequently, the quantities of interest are  $\tilde{\mathbf{H}}(x, y)$  and  $\theta(x, y)$ . To keep track of these quantities, denoting the magnitude, direction, and phase lag, we can use vector phasors.

A phasor [6, 26] is a complex quantity which completely defines the magnitude and phase shift for  $\bar{\mathbf{H}}(x, y, t)$ . Figure 1.2 illustrates how the magnitude and phase are defined through the complex number. The magnitude is represented by the radius of the circle, and the phase is the angle which the complex vector makes with the real axis. Thus, the vector phasor  $\mathbf{H}$  and the explicit time dependent field  $\bar{\mathbf{H}}(x, y, t)$  are related in the following way

$$(1.1) \quad \bar{\mathbf{H}}(x, y, t) = \text{Re}(\mathbf{H}(x, y)e^{i\omega t}) = \text{Im}(\mathbf{H}(x, y)e^{i(\omega t + \pi/2)})$$

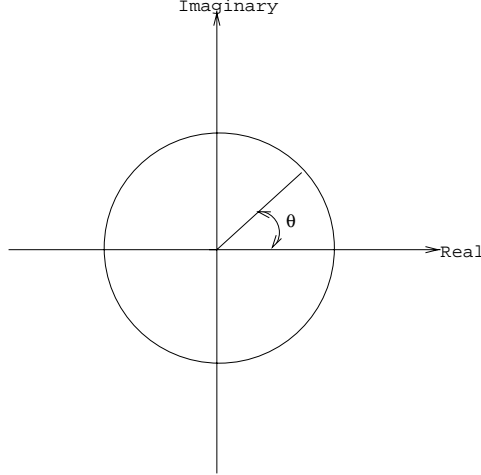


FIG. 1.2. *Illustration of Phasor Notation*

in which all of the phase information and direction is captured in the complex vector phasor  $\mathbf{H}$ . For this reason, in the remainder of the paper we will assume no explicit time dependence in the fields examined, but instead consider the fields to be complex vector phasors, denoted  $\mathbf{H}$ ,  $\mathbf{B}$ , etc, and account for the time dependence of the fields through phase shifts contained in the phasors.

**1.3. Formulation of Forward Problem.** Maxwell's equations are the basis of the derivation in the forward problem. However, since we are expressing the various fields in terms of phasors which depend on space coordinates but not explicitly on time, we want to express time-dependent Maxwell's equations in terms of phasors. We first examine the explicit time-dependent Maxwell's equations. The usual system as derived from first principles (e.g., Coulomb's law, the Lorentz transformation and relativity theory - see [10]) is written as

$$(1.2) \quad \nabla \cdot \overline{\mathbf{B}} = 0,$$

$$(1.3) \quad \nabla \cdot \overline{\mathbf{D}} = \rho,$$

$$(1.4) \quad \nabla \times \overline{\mathbf{E}} = -\frac{\partial}{\partial t} \overline{\mathbf{B}},$$

and

$$(1.5) \quad \nabla \times \overline{\mathbf{H}} = \overline{\mathbf{J}} + \frac{\partial}{\partial t} \overline{\mathbf{D}}.$$

To examine the relationship between the explicit time-dependent Maxwell's equations and Maxwell's equations in terms of phasors, we examine the relationship in equation (1.1). Based upon this relationship, the time derivative for  $\overline{\mathbf{H}}(x, y, t)$  (and similarly other fields) is given by

$$(1.6) \quad \frac{\partial}{\partial t} \overline{\mathbf{H}}(x, y, t) = \omega \text{Re}(i\mathbf{H}(x, y)e^{i\omega t}) = \omega \text{Im}(i\mathbf{H}(x, y)e^{i(\omega t + \pi/2)}).$$

Substituting the appropriate form of equations (1.1) and (1.6) into equations (1.2) - (1.5), we obtain the completely equivalent phasor form of Maxwell's equations

$$(1.7) \quad \nabla \cdot \mathbf{B} = 0,$$

$$(1.8) \quad \nabla \cdot \mathbf{D} = \rho,$$

$$(1.9) \quad \nabla \times \mathbf{E} = -i\omega\mathbf{B},$$

and

$$(1.10) \quad \nabla \times \mathbf{H} = \mathbf{J} + i\omega\mathbf{D}.$$

Thus equations (1.7) - (1.10) hold for our entire “window”, denoted  $\Omega$ .

We could further simplify equations (1.7) - (1.10) in the example under investigation by making some observations. First of all, since our system is considered to be electrically neutral, the internal electric charge density  $\rho$  equals zero. Secondly, by examining the conductivity  $\sigma$  of aluminum and copper and by using Ohm’s law

$$\mathbf{J} = \sigma\mathbf{E},$$

we can argue  $\mathbf{J} \approx 10^7\mathbf{E}$ . On the other hand, the constitutive law

$$(1.11) \quad \mathbf{D} = \epsilon\mathbf{E},$$

indicates  $\mathbf{D} \approx 10^{-11}\mathbf{E}$ . We are using a frequency of  $60Hz$  in our problem which yields an angular frequency of approximately  $3 \times 10^2 rad/sec$ , and thus  $\omega\mathbf{D} \approx 10^{-9}\mathbf{E}$ . Consequently, in the sample and conducting sheet  $\mathbf{J} \gg \omega\mathbf{D}$  which implies we could assume  $\omega\mathbf{D} \approx 0$  in both the sample and conducting sheet in equation (1.10). In other words, the term  $\omega\mathbf{D}$  on the right side of equation (1.10) is only significant in the air. Thus the form of Maxwell’s equations we will use in the computations are given by

$$(1.12) \quad \nabla \cdot \mathbf{B} = 0,$$

$$(1.13) \quad \nabla \cdot \mathbf{D} = 0,$$

$$(1.14) \quad \nabla \times \mathbf{E} = -i\omega\mathbf{B},$$

and

$$(1.15) \quad \nabla \times \mathbf{H} = \mathbf{J} + i\omega\mathbf{D}$$

where, as noted above, the term  $i\omega\mathbf{D}$  is only significant in the air. However, we shall retain this term in all of  $\Omega$  since this is done in the commercial simulator (Ansoft) that we employ below.

Based upon equation (1.12) and vector null identities, we can represent  $\mathbf{B}$  as the curl of a vector potential  $\mathbf{A}$ ,  $\mathbf{B} = \nabla \times \mathbf{A}$ , where  $\mathbf{A}$  is referred to as the magnetic vector potential. The forward problem will be formulated in terms of this magnetic vector potential from which we can derive both the magnetic field  $\mathbf{H}$  and magnetic flux density  $\mathbf{B}$ . Accordingly, we want to combine Maxwell’s equations to obtain equations in conjunction with boundary conditions which completely determine the behavior of the magnetic vector potential  $\mathbf{A}$  in  $\Omega$  defined by

$$\Omega = \{(x, y, z) \in R^3 : 0mm \leq x \leq 50mm, -35mm \leq y \leq 35mm\}.$$

Using the identity  $\mathbf{B} = \nabla \times \mathbf{A}$  in equation (1.14), we have

$$\nabla \times \mathbf{E} = -i\omega(\nabla \times \mathbf{A}) \quad \text{or} \quad \nabla \times (\mathbf{E} + i\omega\mathbf{A}) = 0.$$

Again if one uses vector null identities, the curl of  $\mathbf{E} + i\omega\mathbf{A}$  being zero implies  $\mathbf{E} + i\omega\mathbf{A}$  can be written as the gradient of a scalar potential, denoted by  $\phi$ . As a result,

$$(1.16) \quad \mathbf{E} = -i\omega\mathbf{A} - \nabla\phi.$$

Finally, we can use equations (1.15) and (1.16) in conjunction with Ohm's law, the constitutive law given by (1.11) and the constitutive law  $\mathbf{H} = \frac{1}{\mu}\mathbf{B}$ , to obtain

$$(1.17) \quad \nabla \times \left( \frac{1}{\mu} \nabla \times \mathbf{A} \right) = \sigma(-i\omega\mathbf{A} - \nabla\phi) + i\omega\epsilon(-i\omega\mathbf{A} - \nabla\phi) \quad \forall x, y \in \Omega.$$

In the above equality, the right side represents the total current density  $\mathbf{J}$  which is made up of the source current density, eddy current density and displacement current density. The source current density  $\mathbf{J}_s$  is due to differences in electric potential; therefore,  $\mathbf{J}_s$  is represented by the term  $-\sigma\nabla\phi$ . The term  $-i\omega\sigma\mathbf{A}$  represents the eddy current density,  $\mathbf{J}_e$ , produced due to a time-varying magnetic field. Finally, the displacement current density,  $\mathbf{J}_d$ , due to time-varying electric fields is given by the term  $i\omega\epsilon(-i\omega\mathbf{A} - \nabla\phi)$ .

Since equation (1.17) contains two unknowns,  $\mathbf{A}$  and  $\phi$ , we need an additional equation to uniquely determine solutions of the system. In the literature [6, pp. 327-328], [14, pp.219-221] a ‘‘gauge’’ is commonly chosen which allows one to uniquely determine both  $\mathbf{A}$  and  $\phi$ . In time-varying problems a gauge satisfying the Lorentz condition

$$(1.18) \quad \nabla \cdot \mathbf{A} + \mu\epsilon \frac{\partial\phi}{\partial t} = 0,$$

is most often imposed. However, based upon the geometry in our test problem,  $\nabla \cdot \mathbf{A}$  can be seen to be zero. This follows since the only nonzero component of  $\mathbf{A}$  is  $A_3$ , the component of  $\mathbf{A}$  in the  $z$  direction (the direction of the current density  $\mathbf{J}$ ). Therefore,  $\nabla \cdot \mathbf{A} = \frac{\partial A_3}{\partial z} = 0$  since we have uniformity in the  $z$  direction. Indeed, this is the Coulomb gauge [14, pp. 221-222] and with this we only need impose an initial condition or an equivalent integral constraint. For this we take the relationship

$$(1.19) \quad I = \int_{cs} \mathbf{J} \cdot \mathbf{n} da = \int_{cs} (\sigma(-i\omega\mathbf{A} - \nabla\phi) + i\omega\epsilon(-i\omega\mathbf{A} - \nabla\phi)) \cdot \mathbf{n} da$$

between the total current  $I$  flowing in the conducting sheet (cs) and the total current density  $\mathbf{J}$  within the conducting sheet. This is the second equation used in the software package Ansoft Maxwell 2D Field Simulator which we use in our computational efforts. Therefore, we have two coupled equations (1.17) and (1.19) in which the magnetic vector potential  $\mathbf{A}$  can be uniquely determined if appropriate boundary conditions on  $\mathbf{A}$  are specified. We remark that the imposition of a gauge often decouples the equations for the potentials  $\mathbf{A}$  and  $\phi$  [14, p.220-222]. In our case, the equations (1.17) and (1.19) remain coupled even in the presence of a Coulomb gauge.

Recall, from Section 1.1 that we assume evenly symmetric  $x$  boundaries due to the symmetry of the crack and the infinite extent of the materials. In other words on the  $x$  boundaries, we assume the fields on both sides of the boundary oscillate in the same direction. To account for the even symmetry, we assign Neumann boundary conditions to these boundaries. In a similar manner, we assume the  $y$  boundaries are ‘‘sufficiently far’’ away from the sample and scanning area to not effect the overall measurements. Indeed,

as one moves farther away from the sample and conducting sheet, the magnetic vector potential  $\mathbf{A}$  tends to zero. Therefore, on the  $y$  boundaries, we assign Dirichlet boundary conditions to indicate the boundary is “sufficiently far” away from the materials so that  $\mathbf{A} \approx \mathbf{0}$ . Therefore, the magnetic vector potential  $\mathbf{A}$  is determined according to

$$\nabla \times \left( \frac{1}{\mu} \nabla \times \mathbf{A} \right) = \sigma(-i\omega \mathbf{A} - \nabla \phi) + i\omega \epsilon(-i\omega \mathbf{A} - \nabla \phi) \quad \forall x, y \in \Omega.$$

and

$$I = \int_{cs} \mathbf{J} \cdot \mathbf{n} da = \int_{cs} (\sigma(-i\omega \mathbf{A} - \nabla \phi) + i\omega \epsilon(-i\omega \mathbf{A} - \nabla \phi)) \cdot \mathbf{n} da$$

with

$$\begin{aligned} \mathbf{A}(x, -35) &= 0 = \mathbf{A}(x, 35) \\ \nabla \mathbf{A} \cdot \mathbf{n}|_{(0,y)} &= 0 = \nabla \mathbf{A} \cdot \mathbf{n}|_{(50,y)}. \end{aligned}$$

**2. Computational Method.** Our goal here is to characterize the geometry of a hidden, i.e., subsurface, crack within a sample. To achieve this goal, we must develop fast and efficient forward computational methods to be used possibly numerous times in the inverse problem formulated below. To this end, we examine reduced order Karhunen-Loueve or Proper Orthogonal Decomposition (POD) techniques.

The POD technique is an attractive order reduction method, because basis elements are formed which span a data set consisting of experimental or numerical simulations in an “optimal” way. Since the POD basis is formed such that each basis captures important aspects of the data set, only a small number of POD basis elements are needed in general to describe the solution [24]. Consequently, the POD method will enable us to formulate a fast forward algorithm which still describes the solution accurately with only a few basis elements.

**2.1. The POD Method.** We summarize the use of the POD method in the context of the least squares inverse problem described in detail in the next section. For further details on the general POD method, we refer the reader to [2, 4, 5, 8, 16, 18, 19, 20, 21, 22, 23, 24] and the extensive list of references contained therein. The first step in forming the POD basis is to collect “snapshots” or solutions across time, space or a varied parameter. In our case, we let  $\mathbf{q}$  be the vector parameter characterizing physical properties of the damage, for example, the length, thickness, depth, center, etc. of the damage. For an ensemble of damages  $\{\mathbf{q}_j\}_{j=1}^{N_s}$ , we obtain corresponding solutions,  $\{\mathbf{A}(\mathbf{q}_j)\}_{j=1}^{N_s}$ , of (1.17), for magnetic vector potentials which we call our “snapshots”. Alternatively, from the solution set  $\{\mathbf{A}(\mathbf{q}_j)\}_{j=1}^{N_s}$ , we can obtain the magnetic fluxes  $\{\mathbf{B}(\mathbf{q}_j)\}_{j=1}^{N_s}$  and instead use these as our “snapshots” if we wish to treat magnetic fluxes as our basic state variable. However, for our explanation, we will consider snapshots on  $\mathbf{A} = (0, 0, A_3)$  and hence our explanation will be for the scalar case. For the vector case, we would simply proceed componentwise [2, 8, 24]. Without loss of generality, we will denote the vector  $\mathbf{A}$  by its scalar nonzero component  $A$ , i.e., the  $A_3$  component of  $\mathbf{A}$ .

As explained in [24], we seek basis elements of the form

$$(2.1) \quad \Phi_i = \sum_{j=1}^{N_s} V_i(j) A(\mathbf{q}_j)$$

where the coefficients  $V_i(j)$  are chosen such that each POD basis element  $\Phi_i$ ,  $i = 1, 2, \dots, N_s$ , maximizes

$$\frac{1}{N_s} \sum_{j=1}^{N_s} |\langle A(\mathbf{q}_j), \Phi_i \rangle_{L^2(\Omega, \mathbb{C})}|^2$$



subject to  $\langle \Phi_i, \Phi_i \rangle_{L^2(\Omega, \mathbb{C})} = \|\Phi_i\|^2 = 1$ . It is thus readily seen using standard arguments that the coefficients  $V_i(j)$  are found by solving the eigenvalue problem

$$CV = \lambda V$$

where the covariant matrix  $C$  is given by

$$[C]_{ij} = \frac{1}{N_s} \langle A(\mathbf{q}_i), A(\mathbf{q}_j) \rangle_{L^2(\Omega, \mathbb{C})}.$$

Since the matrix  $C$  is a Hermitian positive semi-definite matrix, it possesses a complete set of orthogonal eigenvectors with corresponding nonnegative real eigenvalues. We order the eigenvalues along with their corresponding eigenvectors such that the eigenvalues are in decreasing order,

$$\lambda_1 \geq \lambda_2 \geq \dots \geq \lambda_{N_s} \geq 0.$$

We then normalize the eigenvectors corresponding to the rule

$$V_i \cdot V_j = \frac{\delta_{ij}}{N_s \lambda_j}.$$

Then the  $i^{th}$  POD basis element is defined by (2.1) where  $V_i(j)$  represents the  $j^{th}$  component of the  $i^{th}$  eigenvector of  $C$ . It can also be shown that  $\{\Phi_i\}_{i=1}^{N_s}$  are orthonormal in  $L^2(\Omega, \mathbb{C})$  and  $span\{\Phi_i\}_{i=1}^{N_s} = span\{A(\mathbf{q}_j)\}_{j=1}^{N_s}$ . Indeed, given any  $A(\mathbf{q}_j)$ , we have

$$A(\mathbf{q}_j) = \sum_{k=1}^{N_s} \alpha_k(\mathbf{q}_j) \Phi_k$$

where

$$\alpha_k(\mathbf{q}_j) = \langle A(\mathbf{q}_j), \Phi_k \rangle_{L^2(\Omega, \mathbb{C})}.$$

We remark that if any of the  $\lambda_i$ 's are zero, say  $\lambda_i = 0$  for  $i = K+1, \dots, N_s$ , then even though the corresponding  $V_i$  are orthogonal (and of course linearly independent), we will have  $span\{\Phi_i\}_{i=1}^K = span\{\Phi_i\}_{i=1}^{N_s}$ . Hence in this case we will only generate  $K < N_s$  linearly independent POD basis elements. We refer the reader to a discussion of the relation between POD basis element formation and the popular singular value decomposition (SVD) methods in linear algebraic methods given in [20], for example.

To determine the reduced number,  $N$ , of POD basis elements required to accurately portray the ensemble of “snapshots”  $\{A(\mathbf{q}_j)\}_{j=1}^{N_s}$ , we compute

$$\sum_{j=1}^N \lambda_j / \sum_{j=1}^{N_s} \lambda_j$$

which represents the percentage of “energy” in  $span\{A(\mathbf{q}_j)\}_{j=1}^{N_s}$  that is captured in  $span\{\Phi_j\}_{j=1}^N$ . The reduced basis consists of only the first  $N$  elements  $\Phi_i$ ,  $i = 1, \dots, N$ , where  $N$  is chosen according to the percentage “energy” desired. From these  $N$  POD basis elements, we obtain the approximation  $A^N(\mathbf{q}_j)$  for  $A(\mathbf{q}_j)$  such that

$$A(\mathbf{q}_j) \approx A^N(\mathbf{q}_j) \equiv \sum_{k=1}^N \alpha_k(\mathbf{q}_j) \Phi_k.$$

To approximate  $A^N(\mathbf{q})$  where  $\mathbf{q}$  is a given parameter *not* in the set  $\{\mathbf{q}_j\}_{j=1}^{N_s}$ , we extend the approximation formula to obtain

$$A^N(\mathbf{q}) = \sum_{k=1}^N \alpha_k(\mathbf{q}) \Phi_k$$

where  $\alpha_k(\mathbf{q})$  is evaluated through interpolation methods. Various interpolation methods may be chosen to evaluate  $\alpha_k(\mathbf{q})$  such as linear interpolation, cubic interpolation, cubic spline interpolation or nearest neighbor interpolation. In the one-dimensional parameter case presented numerically in this paper, we use a Matlab interpolation function *interp1* in which the linear interpolation method is chosen. In other words, for  $\mathbf{q} = q$  (the scalar case)

$$\alpha_k(q) \equiv \alpha_k(q_j) + (\alpha_k(q_{j+1}) - \alpha_k(q_j)) \frac{q - q_j}{q_{j+1} - q_j}$$

where there exists  $j$  in  $\{1, \dots, N_s - 1\}$  such that  $q_j < q < q_{j+1}$ .

Once we have the solution  $A^N(\mathbf{q})$ , we can recapture the explicit time dependence by referring to the formula (1.1) in Section 1.2 given by

$$\overline{\mathbf{A}}(x, y, t) = \text{Re}(\mathbf{A}(x, y)e^{i\omega t}).$$

**2.2. Inverse Problem.** Using the methodology presented in the previous section for calculating the magnetic vector potential  $A$  given specific crack parameters, we shall try to identify these crack parameters. In identifying the geometry of a crack, we would like to estimate the length, thickness, center and depth of a crack within a sample. To determine the feasibility of this task and to illustrate the use of the reduced model methodology, we first try to estimate a single parameter, say length or thickness, while assuming the values of the other parameters are known quantities. If this can be successfully done, further efforts at estimating two or more parameters can be pursued in a similar manner.

**2.2.1. Least Squares Criterion.** In our trial runs, we assume we have access to various types of data, such as the  $\mathbf{A}$  field or the  $\mathbf{B}$  field, in various points  $(x_i, y_i)$  of space, which we call the set  $\Psi$ . We compare and contrast the accuracy to which we can estimate the given parameter or parameters based upon the field, i.e.,  $\mathbf{A}$  or  $\mathbf{B}$ , to which we have access as well as what an appropriate choice of the points in  $\Psi$  should be.

For example, we assume first that the unknown parameter set contains only values of the parameter lengths  $l$ . That is, we want to estimate only the length of the crack assuming the thickness, center, and depth are fixed quantities. Given an arbitrary length  $l$ , we can generate a solution  $A^N(l)$ , the computed solution  $A^N$  as described in Section 2.1. We can compare the computed solution to the experimental or simulated data  $\hat{A}(l^*)$  for the exact parameter value  $l^*$ . For the examples presented here, we choose the parameter values for equations (1.17) and (1.19) given in Table 2.1. However, for the system values given, the order of magnitude of  $A$  is  $10^{-8} \frac{Wb}{m}$ ; therefore it is desirable to scale both the data and the computed solution to achieve a more accurate estimation. If the data is below the desired tolerance of the optimization routine used (the Matlab-based routine *nelder* in our case), the converged estimated value will be the initial guess. Therefore, in this case, we want to minimize the least squares criterion

$$(2.2) \quad J(l) = \sum_{i=1}^n \sum_{j=1}^m |10^8 A^N(x_i, y_j, l) - 10^8 \hat{A}(x_i, y_j, l^*)|$$

over the set of all possible length values  $l$  where  $(x_i, y_j), i = 1, \dots, n; j = 1, \dots, m$  are points in the set  $\Psi$ . The set  $\Psi$ , in our trial runs, varies from a set of points uniformly discretizing all of  $\Omega$  to simply one line of

TABLE 2.1  
Parameters Used in Equation (1.17) for Computational Results

Parameter	Value
$\omega$	$2\pi f$
$f$	$60Hz$
$\sigma_{al}$	$3.72 \times 10^7 \frac{S}{m}$
$\sigma_{cu}$	$5.80 \times 10^7 \frac{S}{m}$
$\sigma_{air}$	$0 \frac{S}{m}$
$I$	$1A$

sample points above the conducting sheet or one line below the sample with a grid spacing of  $0.5mm$  in both the  $x$  and  $y$  direction. If we assume we have access to the values of  $\hat{A}$  in all of  $\Omega$ , in other words, values in the conducting sheet and the sample as well the air above the conducting sheet, below the sample, and in between the sample and conducting sheet, the set  $\Psi$  is thus given by

$$\Psi = \{(x_i, y_j) \in \Omega | x_i = (0.5i)mm, i = 0, \dots, 100; \\ y_j = (0.5j - 35)mm, j = 0, \dots, 140\}.$$

If instead we (more realistically) assume we only have access to values on a line  $1mm$  above the conducting sheet, the set  $\Psi$  is given by

$$\Psi = \{(x_i, y) \in \Omega | x_i = (0.5i)mm, i = 0, \dots, 100; y = 2mm\}$$

(the top of the conducting sheet is at  $y = 1mm$ ). We can describe  $\Psi$  similarly for other choices of data sets.

In most experimental settings, we do not have access to measurements of the magnetic vector potential  $\mathbf{A}$ , but instead to those of the magnetic flux density  $\mathbf{B}$ . In this case, we first compute  $\mathbf{A}^N(l)$  for a given  $l$  in the manner described in Section 2.1. To find the computed magnetic flux density  $\mathbf{B}^N(l)$ , we simply use the definition

$$\mathbf{B}^N(l) = \nabla \times \mathbf{A}^N(l).$$

In general, it is not necessary to use the entire  $\mathbf{B}$  field, but instead we can use only one component of the  $\mathbf{B}$  field, either the  $x$  component,  $B_1$ , or the  $y$  component,  $B_2$ . If we are using the  $x$  component of  $\mathbf{B}$ , our least squares criterion would be

$$(2.3) \quad J(l) = \sum_{i=1}^n \sum_{j=1}^m |10^8 B_1^N(x_i, y_j, l) - 10^8 \hat{B}_1(x_i, y_j, l^*)|^2;$$

whereas, if we use the  $y$  component of the  $\mathbf{B}$  field, the criterion would be

$$(2.4) \quad J(l) = \sum_{i=1}^n \sum_{j=1}^m |10^8 B_2^N(x_i, y_j, l) - 10^8 \hat{B}_2(x_i, y_j, l^*)|^2$$

where  $(x_i, y_j) \in \Psi$ . We minimize one of the three criteria, (2.2), (2.3), and (2.4), along various sets  $\Psi$  and determine which criterion allows us to most accurately determine the unknown parameter  $l$  while allowing for the limitations of the given set  $\Psi$ . We can estimate other unknown parameters in a similar manner by replacing  $l$  by  $\mathbf{q}$  in the above equations where  $\mathbf{q}$  represents the entire set of unknown vector parameters.

**2.2.2. Noise Generator.** In the samples provided, simulated data was used to represent experimental data  $\hat{A}$ ,  $\hat{B}_1$ , or  $\hat{B}_2$ , depending upon the specific trial run. To obtain the simulated data, we specified the parameters  $\mathbf{q}^*$  for a crack and generated the solution based upon these exact parameters using the commercial software Ansoft Maxwell 2D Field Simulator. Again, the goal is to recapture these parameters by minimizing one of the cost functions given above. However, when using actual experimental data, we most often have random error in the measurements taken. To simulate this random error, we add random noise to the simulated data to test our methodology in the presence of noise and to give a more reasonable demonstration of how our algorithm might perform on experimental data.

To generate the noise, we use the Matlab function *randn* which generates a normally distributed set of random numbers with mean 0 and variance 1. A normally distributed set of random numbers has a 65% certainty of being within 1 standard deviation, 95% certainty of being within 2 standard deviations and 99.7% certainty of being within 3 standard deviations of the mean. In other words, there is a 65% chance the Matlab function *randn* will return a number in the interval  $(-1, 1)$ , 95% chance of returning a number in the interval  $(-2, 2)$  and a 99.7% chance of producing a number in the interval  $(-3, 3)$ . Therefore, we can control the amount of noise in the simulated data by scaling the certainty intervals.

For example, assume we have generated the solution  $\hat{A}(\mathbf{q}^*)$  given exact parameters  $\mathbf{q}^*$ . Furthermore, assume we desire to be 95% certain that the noise generated to be added to this solution is within 1% of the actual data  $\hat{A}(\mathbf{q}^*)$ . At this level of noise, we want to scale the interval  $(-2, 2)$  to  $(-0.01, 0.01)$ . Therefore, letting

$$\epsilon_1 = 0.005 * randn,$$

the data,  $\tilde{A}$ , is given by

$$\tilde{A}(\mathbf{q}^*) = \hat{A}(\mathbf{q}^*)(1 + \epsilon_1).$$

Similarly, if we instead want to be 99.7% certain of noise within 1% of the simulated data, we scale the interval  $(-3, 3)$  to  $(-0.01, 0.01)$  or let

$$\epsilon_2 = 0.0033 * randn.$$

As previously, the data at this noise level is given by

$$\tilde{A}(\mathbf{q}^*) = \hat{A}(\mathbf{q}^*)(1 + \epsilon_2).$$

In the trials we performed, we simulated corrupted experimental data by generating noise at a 1% relative noise level with both 95% certainty and 99.7% certainty as discussed above as well as noise at a 5% and 10% relative noise level with both 95% certainty and 99.7% certainty.

**2.3. Results with Test Examples.** In determining the geometry of the crack in our simulations, we focus first on determining the length of the damage and then separately the thickness of the damage. Various trials are performed in each case. In a specific trial run, ten different data sets (exact data with ten different sets of added random noise) are used where the relative noise is chosen either at a 10%, 5%, or 1% noise level with a confidence level of either 95% (2 standard deviations) or 99.7% (3 standard deviations). Details of each trial run can be found in [3]. A summary of the results will be given in this section.

**2.3.1. Determining the Length of the Damage.** The first step in determining the length of the damage is to generate an ensemble of damages with various crack lengths  $\{l_j\}_{j=1}^{N_s}$  to be used in forming the POD basis. In generating the damages for the examples reported on here, we used crack lengths varying from  $0mm$  to  $4mm$  in increments of  $0.2mm$  while keeping the thickness of the crack fixed at  $2mm$  ( $N_s = 21$ ). We then used the commercial software Ansoft Maxwell 2D Field Simulator to generate the snapshots  $\{A(l_j)\}_{j=1}^{21}$ . Based upon the calculations discussed in Section 2.1, 99.99% of the energy of the system was captured with a single basis element. Table 2.2 gives the amount of energy captured when using  $N$  basis elements up to  $N = 10$ .

TABLE 2.2  
*Energy Captured with  $N$  Basis Elements using Snapshots of  $A$  on Length*

$N$	Energy Captured
1	0.99999469355655
2	0.99999998707290
3	0.9999999918539
4	0.9999999978293
5	0.9999999987493
6	0.9999999990451
7	0.9999999992129
8	0.9999999993439
9	0.9999999994409
10	0.9999999995308

To test the inverse methodology, we first try to identify the length of the damage,  $l^* = 1.3mm$ , by using the criterion given in expression (2.2). We ran the inverse problem using 1, 2, 3, 4 and 5 reduced POD basis elements with data containing no noise taken over the entire discretized region  $\Omega$ . There was no noticeable difference between using 4 and 5 basis elements; hence we chose to use 4 POD basis elements in our solution approximation.

Based upon the results ([3, Appendix A.1]), we can conclude that under the assumption that we have access to the magnetic vector potential  $A$  in all of  $\Omega$ , we did a good job of estimating the crack length even when the data contained 5% relative noise. When no noise is added, we obtained an estimated length of  $1.2999mm$ . At the 99.7% confidence level with 5% random relative noise, we obtain an average length,  $\bar{l}$ , of  $1.3160mm$  with variance  $0.0019mm^2$ . (Here and in all results given below, the reported results involve the length or thickness estimates averaged over 10 trial runs.) In actuality, however, we only have access to data in the regions of air above the conducting sheet or below the sample. Therefore, the inverse problem was next carried out using “data” in just these regions. The results ([3, Appendices A.2 & A.7]) illustrate that we still do a reasonable job estimating the crack length. For example, assuming we have access to data in the air above the conducting sheet, we obtain an average length of  $\bar{l} = 1.2504mm$  with a variance of  $0.0094mm^2$  when 5% relative noise is added at the 99.7% confidence level. With no noise added, the estimated length is  $1.2997mm$ .

Although technically it is possible to have access to data in the entire region of air, typically data is taken on only one or two lines above the conducting sheet or below the sample. When running the inverse problem on just a few lines above the conducting sheet or below the sample, the inverse algorithm did *not* perform well, especially for data containing noise at the 5% level. The results ([3, Appendices A.3-A.6,

A.8-A.11]) indicate that if there is a considerable amount of noise (5% noise level in our case), it is not feasible to accurately estimate the crack length using the magnetic vector potential  $A$ . For example, if we have access to data on just one line above the conducting sheet, we obtain a good estimate of  $1.3008mm$  when no noise is added; however, when 5% relative noise is added at the 99.7% confidence level, the average estimated length is  $1.3873mm$  with a variance of  $0.7655mm^2$ . When adding only 1% relative noise at the 99.7% confidence level, we obtain an average estimated length of  $1.2804mm$  with a variance of  $0.0272mm^2$ . Although we obtain better results at a smaller noise level, the results are not as accurate as one would like and the method would be unacceptable in practice.

As we have already noted, in experimental situations one does not have access to the magnetic vector potential. Instead, one only has access to the magnetic flux density or the magnetic field. With this in mind, we repeated the computational tests reported in [3, Appendix A] with the exception of using the criteria given by expressions (2.3) and (2.4). Using  $B_1$  data or the criterion (2.3), the results ([3, Appendix B]) were no better than when we used the magnetic vector potential. Using data on one line above the conducting sheet, the average length obtained was  $1.2223mm$  with a variance of  $0.4715mm^2$  at the 5% noise level with 99.7% confidence. On the other hand, when we used  $B_2$  data ([3, Appendix C]), criterion (2.4), the inverse problem produced remarkably accurate results; estimated lengths were accurate to an order of  $10^{-3}$  even with 5% relative noise. However, the most notable observation in using  $B_2$  data is the low variation in results even at the 5% and 10% relative noise level. Using data on a single line above the conducting sheet with 10% relative noise at a 99.7% confidence level, an average estimated length of  $1.2977mm$  was obtained with a variance of  $0.3237 \times 10^{-4}mm^2$ . Based upon these results, we could quite accurately estimate a given length of a crack even if the data contained a considerable amount of noise. Therefore, we concluded that even when scanning along a single line, when using the  $y$  component of the magnetic flux density, we can accurately recapture the length of a crack within a sample. Scanning along multiple lines or over the whole region provided only marginal improvements in the estimated length; the improvements were not sufficiently substantial to warrant the extra time or money required to obtain the extra data.

The results above were produced using snapshots of the magnetic vector potential. We also took snapshots (with which we formed POD basis elements) on the  $y$  component of the magnetic flux density,  $B_2$ , and performed the analysis again using the criterion (2.4) ([3, Appendix D]). Although there was a quite notable difference in the energy captured in  $N$  basis elements (see Table 2.3), the inverse problems still exhibited the same consistency and accuracy as seen previously. One comparison we can make between using POD elements resulting from snapshots of  $A$  versus snapshots of  $B_2$  in the inverse problem is that when using the snapshots on  $A$ , the estimated length was normally an overestimate. Conversely, using the POD elements resulting from snapshots on  $B_2$  usually yielded an underestimate of the length. For example, when taking snapshots on  $A$  to generate the POD basis elements, we estimated an average length of  $1.3014mm$  with variance  $0.9653 \times 10^{-5}mm^2$  in the inverse problem when using data on a single line above the conducting sheet with 5% relative noise. On the other hand, if we again use data on a single line above the conducting sheet with 5% relative noise added, we estimate an average length of  $1.2999mm$  with variance  $0.1017 \times 10^{-4}mm^2$  when the POD basis elements are generated with  $B_2$  data. Despite this fact, there seems to be no other apparent difference in using the snapshots on  $A$  to generate the basis elements as opposed to using the snapshots on  $B_2$  to generate the basis elements, as long as one uses the criterion (2.4) in the inverse problem calculations.

**2.3.2. Determining the Thickness of the Damage.** Proceeding as we did in estimating the length of a damage, we generated an ensemble of crack thicknesses (with crack length fixed at  $2mm$ ) ranging from

TABLE 2.3  
*Energy Captured with  $N$  Basis Elements using Snapshots of  $B_2$  on Length*

$N$	Energy Captured
1	0.95752844126957
2	0.98938760682215
3	0.99515414870549
4	0.99680555604825
5	0.99749219883487
6	0.99789119249012
7	0.99822617546932
8	0.99853187498393
9	0.99871258779223
10	0.99888757131260

0mm to 4mm in increments of 0.2mm,  $\{h_j\}_{j=1}^{21}$  with associated solutions  $\{A(h_j)\}_{j=1}^{21}$ . Similar to our findings when taking snapshots on the length of a damage, 99.99% of the energy was captured in a single basis element (see Table 2.4).

TABLE 2.4  
*Energy Captured with  $N$  Basis Elements using Snapshots of  $A$  on Thickness*

$N$	Energy Captured
1	0.99999446453503
2	0.9999999666469
3	0.999999993584
4	0.9999999961479
5	0.9999999972048
6	0.9999999980054
7	0.9999999984470
8	0.9999999987779
9	0.9999999990521
10	0.9999999992316

Based upon the results on characterizing the length of the damage, we only considered snapshots of the magnetic vector potential  $A$  with  $B_2$  data in the inverse problem. When estimating the length of the damage in the previous section, only 4 basis elements were required to achieve an estimate with an accuracy of order  $10^{-3}mm$ . However, even though 99% of the energy is captured in a single basis element regardless of whether we snapshot on  $A$  or  $B_2$  (Tables 2.4 and 2.5), more basis elements (at least 8) were required to achieve the same level of accuracy when estimating the thickness of the damage. Therefore, we used 9 POD basis elements. Although more basis elements were used, the total time required to recapture the true thickness (1.3mm) of the crack was still only 8 seconds. Furthermore, the results ([3, Appendix E]) when using 9 POD basis elements were still accurate even in the presence of 10% noise. For example, an average thickness of 1.3041mm with variance  $0.2883 \times 10^{-4}mm^2$  was estimated at the 10% relative noise level at a 99.7% confidence level. Thus, just as in estimating the length of a crack, we can also recapture the thickness

TABLE 2.5  
*Energy Captured with  $N$  Basis Elements using Snapshots of  $B_2$  on Thickness*

$N$	Energy Captured
1	0.99488023435913
2	0.99728234129540
3	0.99799825670140
4	0.99836722535293
5	0.99870058186819
6	0.99896958827131
7	0.99911070207772
8	0.99923141472559
9	0.99934263323537
10	0.99944776176825

of a crack quite accurately and efficiently.

**3. Conclusion.** In this paper, we began by formulating a two-dimensional test problem to be used in locating and characterizing the geometry of a subsurface damage within a sample of material. This two-dimensional problem was argued to be a reasonable approximation to a typical three-dimensional problem under certain assumptions. We then explained the forward problem describing the behavior of the magnetic vector potential in this test problem and discussed computational methods to be used in solving the forward problem. In order to quickly and efficiently obtain results in the inverse problem, the computational methods for the forward problem must be fast and accurate. Therefore, we chose to use the reduced order POD technique in the forward problem, allowing us to use less than 10 basis elements in each of the examples tested to date. Consequently, we were able to provide a fast forward algorithm. Moreover, the POD basis elements were formed so that we captured at least 99% of the energy in these few basis elements, making the forward algorithm accurate as well as fast.

We then outlined the implementation of the inverse problem and results. While the methods did not seem to be robust when using  $A$  data or  $B_1$  data in the inverse algorithm, the methods were robust, even in the presence of 10% relative noise, when using  $B_2$  data regardless of whether we snapshot on the magnetic vector potential or the magnetic flux density. Furthermore, performing multi-line scans or using full region data improve results only marginally over a single line scan and hence do not warrant the extra effort and time in collecting more extensive data sets. A *significant* finding regarding reduction in computational time can be summarized as follows. If one were to use a software package such as Ansoft's Maxwell 2D Field Simulator to calculate the forward problem each time it is required in the inverse problem, it would take approximately 5-10 minutes for a *single* forward solve and hence any inverse algorithm based on this forward solver would require hours of time for the optimization problem. In using the reduced order POD methodology for the forward problem, the *entire inverse problem* takes approximately 8 seconds, less than  $\frac{1}{30}$  the time required for a *single forward simulation* using Ansoft. As a forward algorithm is called numerous times, this is a substantial reduction in time required. Most of the extensive computational time is required only in the initial collection of snapshots. Hence, all of these computations would take place prior to implementation in a practical setting. Therefore, using data collected on a single line above the conducting sheet or below the sample, we are able to estimate the length or thickness of a damage in a small amount of time. This



suggests that a portable SQUID type sensing device, when coupled with reduced order modeling in the inverse problem, might be plausible in practical damage detection applications.

The results summarized in this note suggest that use of the POD based approximation methods in electromagnetic eddy current technique inverse problems for damage is a viable approach. We are therefore continuing our efforts with damages requiring more than one-dimensional parameterization. Our earlier findings in this direction are most encouraging. We are also exploring use of these techniques in geometries requiring 3D formulations.

## REFERENCES

- [1] J.A. ATWELL AND B.B. KING, *Reduced order controllers for spatially distributed systems via proper orthogonal decomposition*, in ICAM Report 99-07-01, VPISU, Blacksburg, VA, July 1999.
- [2] H.T. BANKS, R.C. DEL ROSARIO AND R.C. SMITH, *Reduced order model feedback control design: Numerical implementation in a thin shell model*, Tech. Rep. CRSC-TR98-27, NCSU, July 1998; IEEE Trans. Auto. Control, to appear.
- [3] H.T. BANKS, M.L. JOYNER, B. WINCHESKI AND W.P. WINFREE, *Evaluation of material integrity using reduced order computational methodology*, Tech. Rep. CRSC-TR99-30, NCSU, Aug. 1999.
- [4] G. BERKOOZ, *Observations on the proper orthogonal decomposition*, in Studies in Turbulence, Springer-Verlag, New York, 1992, pp. 229-247.
- [5] G. BERKOOZ, P. HOLMES AND J.L. LUMLEY, *The proper orthogonal decomposition in the analysis of turbulent flows*, Annual Review of Fluid Mechanics, 25 (1993), pp. N5:539-575.
- [6] D.K. CHENG, *Field and Wave Electromagnetics*, Addison-Wesley, Reading, 1989.
- [7] A. COCHRAN, G.B. DONALDSON, C. CARR, D. MCA. MCKIRDY, M.E. WALKER, U. KLEIN, J. KUZNIK AND A. McNAB, *Advances in the theory and practice of SQUID NDE*, Review in Progress in QNDE, 15 (1996), pp. 1151-1158.
- [8] R.C. DEL ROSARIO, *Computational Methods for Feedback Control in Structural Systems*, PhD thesis, N.C. State University, 1998.
- [9] G.B. DONALDSON AND D. MCA. MCKIRDY, *The use of SQUIDS for nondestructive evaluation*, in SQUID Sensors: Fundamentals, Fabrication and Application, 1996, pp. 599-628.
- [10] R.S. ELLIOTT, *Electromagnetics: History, Theory and Applications*, IEEE Press, New York, 1993.
- [11] G.L. FITZPATRICK, D.K. THORNE, R.L. SKAUGSET, E.Y.C. SHIH AND W.C.L. SHIH, *Magneto-optic/eddy current imaging of aging aircraft: A new NDI technique*, Materials Evaluation, 1993, pp. 1402-1407.
- [12] T.W. GUETTINGER, K. GROTZ AND H. WEZEL, *Eddy current imaging*, Materials Evaluation, April 1993, pp. 444-451.
- [13] N.C. HAYWOOD AND J.R. BOWLER, *Eddy-current imaging of buried cracks by inverting field data*, IEEE Trans. On Magnetics, 28, No. 2, pp. 1336-1339.
- [14] J.D. JACKSON, *Classical Electrodynamics*, 2nd ed., John Wiley and Sons, New York, 1975.
- [15] W.G. JENKS AND J.P. WIKSWO JR., *Review article: SQUIDS for nondestructive evaluation*, Journal of Physics D: Applied Physics, 30 (1997), pp. 293-323.
- [16] K. KARHUNEN, *Zur spektral theorie stochastischer prozesse*, Ann. Acad. Sci. Fennicae, Ser. A1 Math Phys., 37 (1946).
- [17] G.M. KEPLER, H.T. TRAN AND H.T. BANKS, *Reduced order model compensator control of species*

- transport in a CVD reactor*, Tech. Rep. CRSC-TR99-15, NCSU, 1999; Optimal Control: Applications and Methods, submitted.
- [18] M. KIRBY AND L. SIROVICH, *Application of the Karhunen-Loeve procedure for the characterization of human faces*, IEEE Transactions on Pattern Analysis and Machine Intelligence, 12 (1990), pp. N1:103-108.
  - [19] M. KIRBY, J.P. BORIS AND L. SIROVICH, *A proper orthogonal decomposition of a simulated supersonic shear layer*, International Journal for Numerical Methods in Fluids, 10 (1990), pp. 411-428.
  - [20] K. KUNISCH AND S. VOLKWEIN, *Control of Burgers' equation by a reduced order approach using proper orthogonal decomposition*, J. Optimization Theory and Applic., to appear.
  - [21] M. LOEVE, *Functions aleatoire de second ordre*, Compte rend. Acad. Sci. (Paris), 1945, p. 220.
  - [22] J.L. LUMLEY, *The structure of inhomogeneous turbulent flows*, Atmospheric Turbulence and Radio Wave Propagation, Moscow: Nauka (1967), pp. 166-178.
  - [23] J.L. LUMLEY, *Stochastic Tools in Turbulence*, Academic Press, New York, 1970.
  - [24] H.V. LY AND H.T. TRAN, *Proper orthogonal decomposition for flow calculations and optimal control in a horizontal CVD reactor*, Tech. Rep. CRSC-TR98-13, NCSU, 1998; Quart. Applied Math, to appear.
  - [25] Y.P. MA AND J.P. WIKSWO, JR., *Imaging subsurface defects using a SQUID magnetometer*, Review of Progress in QNDE, 12A (1993), pp. 1137-1143.
  - [26] Maxwell 2D Field Simulator Version 6.5.04 - Technical Notes, 1997 Ansoft Corporation, pp. 14-16.
  - [27] D. MCA. MCKIRDY, A. COCHRAN, G.B. DONALDSON AND A. McNAB, *Forward and inverse processing in electromagnetic NDE using SQUIDS*, Review of Progress in QNDE, 1996, pp. 347-354.
  - [28] D.K. THORNE, G.L. FITZPATRICK, E.Y.C. SHIH AND W.C.L. SHIH, *Aircraft inspection with the magneto-optic/eddy current imager - a new technology*, presented at the ATA NDT Forum, Long Beach, CA, Sept. 10-12, 1991.
  - [29] M. VAUHKONEN, J.P. KAIPIO, E. SOMERSALO AND P.A. KARJALAINEN, *Electrical impedance tomography with basic constraints*, Inverse Problems, 13 (1997), pp. 523-530.
  - [30] H. WIENSTOCK, *A review of SQUID magnetometry applied to nondestructive evaluation*, IEEE Transactions on Magnetics, 27, No. 2 (1991), pp. 3131-3236.
  - [31] B. WINCHESKI, J. FULTON, S. NATH, M. NAMKING AND J. SIMPSON, *Self-nulling eddy current probe for surface and subsurface flaw detection*, Materials Evaluation, 52, No. 1 (1994), pp. 22-26.
  - [32] B. WINCHESKI, J. FULTON, S. NATH AND M. NAMKUNG, *Analysis of eddy current distribution and resulting flaw detection mechanism for self-nulling probe*, Review of Progress in Quantitative NDE, 14A (1995), pp. 291-298.